Banerjee and Bera
Journal of Electrical Systems and Inf Technol (2022) 9:20
https://doi.org/10.1186/s43067-022-00060-3

Journal of Electrical Systems and Information Technology

RESEARCH **Open Access**

Online equivalent parameter estimation using BPANN controller with low-frequency signal injection for a sensorless induction motor drive

Tista Banerjee* and Jitendra Nath Bera

*Correspondence: tista.banerjee@gmail.com

Department of Applied Physics, University of Calcutta, 92 APC Road, Kolkata 700009, India

Abstract

The development of a sensorless induction motor drive is elaborated in this paper with a unique feature of online estimation of equivalent circuit parameters (ECPs) during its running condition. The cases like temperature rise of the motor, change in drive speed due to sudden changes in its loading, or even in supply voltage are the sources of error in accurate ECPs evaluation. The indirect field-oriented control (IFOC) scheme is adopted in its controller to deal with these challenges. The drive controller is designed with a model reference adaptive system (MRAS) having two models—one is the plant model to estimate the ECPs during running conditions while the other one is the reference model. The H-G diagram method is utilized in the reference model to estimate the reference ECPs (ECP_R) before starting without the need of performing any physical tests on the motor. During the transition period of the drive, the feedback signal is fed to the reference model to generate the ECP_R. The technique of the backpropagation algorithm with an artificial neural network (BPANN) is utilized in the plant model while its weight and gain parameters are tuned with the reference ECPs. The Adam rule is utilized for fast convergence of the BPANN weights during the transition period while stator temperature and speed feedback enhance the overall accuracy in ECPs. A discrete-time low-frequency signal injection-based resistance assessment and sensorless speed estimation method to determine inductances are adopted for minimizing the ECPs errors. The results from MATLAB-based simulation and a hardware prototype using a DSPIC microcontroller with different running conditions show the efficacy of the proposed algorithm.

Keywords: IFOC, Parameter estimation, Space vector modulation, H-G diagram, BPANN, Adam, Small-signal injection, Speed estimation

Introduction

Nowadays IFOC schemes are generally adopted in ASD controllers of IM for better speed control, both during its transient and steady-state running [1]. Determination of accurate values of ECPs is essential based on which the time constant, slip speed relationship, d-q axis currents, etc., can be evaluated for successful implementation of IFOC. But during running conditions some of the ECPs, stator, and rotor resistances,

© The Author(s) 2022. **Open Access** This article is licensed under a Creative Commons Attribution 4.0 International License, which permits use, sharing, adaptation, distribution and reproduction in any medium or format, as long as you give appropriate credit to the original author(s) and the source, provide a link to the Creative Commons licence, and indicate if changes were made. The images or other third party material in this article are included in the article's Creative Commons licence, unless indicated otherwise in a credit line to the material. If material is not included in the article's Creative Commons licence and your intended use is not permitted by statutory regulation or exceeds the permitted use, you will need to obtain permission directly from the copyright holder. To view a copy of this licence, visit http://creativecommons.org/licenses/by/4.0/.

in particular, are getting changed due to harmonics heating effect, skin effect, change in load, and under-voltage running reasons [2, 3]. These changes in ECPs are the sources of errors resulting in the inaccurate generation of gate triggering pulses and hence proper control of speed could not be achieved. In IFOC-based VSI-IM drive, accurate estimation of ECPs during steady-state and transient conditions is an age-old challenge. Moreover, high-speed DSP-based processors are also being utilized to process these ECPs data following the IFOC algorithm with the feedback of speed, temperature, loading conditions, etc. [4–8].

For estimation and optimization of IM parameters, various conventional methods like spectrum analysis and sinusoidal signal perturbation as well as intelligent control algorithms like GA, PSO and their hybrid form, bacterial foraging, anthill, GSA, etc., offline methods [9, 10] are proposed. These algorithms are easy to implement and support multi-objective optimization but the convergence time is large, which makes these algorithms incapable of online application. To overcome these problems, FLCs are used but the rule-based FLC requires all the possible variations of the motor condition. Hence FLC could not be able to produce a satisfactory result where all of this information is not available. Various other state observers like EKF, Luenberger observer and its extended form, polynomial regression method [11], etc., can estimate parameters efficiently but higher complexities make these algorithms time-consuming and becoming difficult for their real-time implementation even with DSP-based processors [3, 4].

In works [12–16], ANN algorithms using high-speed DSP-based processors are proposed as these algorithms perform faster than other heuristic ones. The efficiency of the ANN algorithm depends upon its structure, chosen optimizer, and training logic. Accordingly, RNNs, LSTM, CNNs, encoder-decoder-based networks, and GNNs are preferred [12]. But these types of network are either unsupervised or self-supervised type for which the training of these NN models is relatively slow and also needs extra memory to hold all the set of sampled data [12–16]. Besides, most of the NN, RNN, and GNN also suffer from exploding and vanishing gradient problems. To minimize these, some improved activation functions like Leaky ReLu [17] and Adam optimizers [18] are chosen to get a fast and stable convergence. However, the activation function like Leaky ReLu does not provide a satisfactory result with RNN.

For close-loop scalar or vector control methods, estimation of speed is very essential and any arrangement for speed sensor mounting makes the drive less reliable and costly. Without these sensors, it is possible to estimate speed from the feedback of stator voltage and current signals, but these processes are complex and their accuracy depends on motor parameters. Various methods have been proposed for sensorless speed estimation like slip calculation, EKF, Luenberger observer, AI, MRAS, sliding mode observers, flux linkage method, back emf method, etc. [19–22].

Temperature variation is the main cause of variation in the stator and rotor resistances. This may lead to inaccurate speed estimation and vector control logic may get detuned. Thus temperature correction of these resistances is essential. Various methods are proposed like dc signal injection, ac signal injection, Goertzel algorithm to the complex current and voltage space vectors, thermal observers, voltage disturbance observers, etc., to estimate the temperature or the stator resistance directly [23–26].

Getting motivated by these, the authors of this paper propose a model reference, the adaptive system-based plant model, where a BPANN-based efficient algorithm is adopted to estimate accurate equivalent circuit parameters. The ECPs are estimated both in pre-starting in off-line mode, during starting transient and running conditions as well in an on-line mode without the requirement of physical tests like no-load and blocked rotor tests. The BPANN-based online estimation scheme is adopted to consider any change in parameters due to changes in the running conditions like temperature variation which in turn makes the drive more accurate and efficient. Adoption of the Adam method [18] makes the tuning of the weight factors of ANN at a faster convergence rate such that this tuning is completed during the starting of the motor irrespective of the capacity of the motor. The H-G [27, 28] method is adopted for the evaluation of ECP_R in the reference model during starting the transient period with the help of nameplate data [29] and the feedback signals of voltage and current. This ECP_R is used to train the BPANN during motors starting transient period. Besides, for diagnosis purposes, a machine monitoring unit is also developed that interfaces with the DSP-based microcontroller and displays all the machine parameters, variables, and feedback values before and during running conditions. The proposed system has the following unique features: (i) The IFOC controller is broadly constituted with two models namely the reference model and the Plant model to generate ECPs independently. (ii) The ECPs have been generated accurately from M_R using motor nameplate data and the H-G diagram method up to the starting transient period. (iii) The BPANN gain parameters of M_P are getting tuned during the starting transient period. After then, ECPs are evaluated during the entire running condition of the motor. (iv) To maintain the accuracy in ECPs evaluation from M_P, the estimation of motor resistance during running conditions as well as temperature using the SSI method as well as rotor speed using the sensorless scheme is adopted. (v) The various parameters during running conditions can be monitored from a remote GUI using its MMU module. This can also be used for diagnosis purposes.

The uniqueness of the proposed work is that an online accurate ECPs estimation scheme is developed with the help of a robust IFOC controller using BPANN based plant model along with their necessary corrections using feedback of sensorless estimated values of speed and motor temperature.

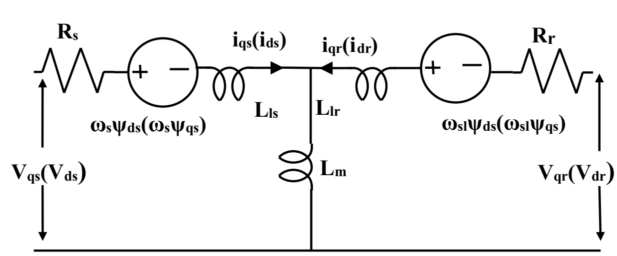

Fig. 1 Per phase equivalent circuit of IM in d-q frame

Proposed IFOC based induction machine drive

Equivalent circuit parameter model of IM

The steady-state per phase equivalent circuit of the IM referred to the stator side in the d-q reference frame is shown in Fig. 1 where R_s, R_r, X_s, X_r, L_s, and L_r represent the stator and rotor resistance, reactive inductances while R_m, X_c, and L_m represent core resistance, reactance, and mutual inductance, respectively. The equivalent impedance of the system is given by Eq. (1)

$$Z_{\mathrm{eq}} = \frac{V_{\mathrm{s}}}{I_{\mathrm{s}}} = (R_{\mathrm{s}} + j\omega_{\mathrm{s}}L_{\mathrm{s}}) + \frac{\left(\frac{R_{\mathrm{r}}}{s} + j\omega_{\mathrm{s}}L_{\mathrm{r}}\right) \times (j\omega_{\mathrm{s}}L_{\mathrm{m}})}{\left(\frac{R_{\mathrm{r}}}{s} + j\omega_{\mathrm{s}}L_{\mathrm{r}}\right) + (j\omega_{\mathrm{s}}L_{\mathrm{m}})} \tag{1}$$

To study the various dynamic conditions during the running of the motor, the IFOC scheme is generally adopted. To implement IFOC, this steady-state per phase equivalent circuit is represented by dynamic equivalent circuit in the synchronously rotating d-q model as shown in Fig. 1, where the stator current I_s is represented by (i_{ds}, i_{qs}) and rotor current I_r as (i_{dr}, i_{qr}), the stator and rotor fluxes by (ψ_{ds}, ψ_{qs}) and (ψ_{dr}, ψ_{qr}), stator and rotor voltages by (v_{ds}, v_{qs}) and (v_{dr}, v_{qr}). The synchronous speed is ω_s and the rotor speed is ω_r.

Proposed schematic for IFOC drive

The schematic diagram of the proposed IFOC of the VSI-IM drive, as shown in Fig. 2, has four major blocks—namely (i) power unit, (ii) control unit, (iii) sensor unit, and (iv) machine monitoring unit (MMU). The power unit is built with IGBTs in the H-Bridge configuration to provide the controlled power output to the IM. The control unit is built with a fast operating DSP microcontroller; the firmware of which estimates the proposed equivalent circuit parameter required to generate triggering pulses following IFOC algorithms with greater accuracy. The IFOC controller logics are described in detail in the following "The IFOC controller schematic" section to generate modulating signal corresponding to the SVM scheme. Accordingly, the generated triggering pulses are fed to the respective IGBTs through their proper gate driver circuit so that the desired speed of the IM can be achieved. To achieve better speed control, the feedback signals of voltage, current, and speed are fed to the IFOC logic. Thus, the sensor unit is equipped with voltage hall sensors for voltage sensing, a current hall sensor for current sensing, and an optical encoder for rotor speed sensing. To have a better understanding of the changes in the internal parameters of IM during ts running conditions, a PC-based data acquisition

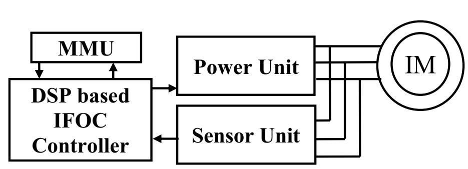

Fig. 2 IFOC based VSI-IM drive prototype model

system is developed where the ECPs from IFOC is communicated serially. The MMU is a PC-based GUI to display, analyze and control various running states by collecting data from the microcontroller using serial communication. This state-of-the-art GUI is extremely helpful in designing and debugging the control algorithm, for initial training of single layer BPANN weight factors, etc. From this GUI, the desired speed can also be set.

The IFOC controller schematic

The adopted IFOC controller schematic with independent paths for the torque and flux control using orthogonal currents i_{ds} and i_{qs} as shown in Fig. 3. The d-q stator currents as reference are generated from flux and torque flow paths using Eq. (2) and (3).

$$\psi_{\mathrm{r}} = L_{\mathrm{m}} i_{\mathrm{ds}}^{*}, i_{\mathrm{ds}}^{*} \triangleq \frac{\psi_{\mathrm{r}}}{L_{\mathrm{m}}}, K_1 = \frac{1}{L_{\mathrm{m}}} \tag{2}$$

$$T_{\mathrm{e}} \simeq \frac{3}{2}\left(\frac{p}{2}\right)\frac{L_{\mathrm{m}}}{L_{\mathrm{r}}}\psi_{\mathrm{r}} i_{\mathrm{qs}}^{*} \triangleq \frac{3p}{4}\frac{L_{\mathrm{m}}^2}{L_{\mathrm{r}}} i_{\mathrm{ds}}^{*} i_{\mathrm{qs}}^{*}, i_{\mathrm{qs}}^{*} = \frac{T_{\mathrm{e}} K_2}{i_{\mathrm{ds}}^{*}}, K_2 = \frac{4L_{\mathrm{r}}}{3pL_{\mathrm{m}}^2} \tag{3}$$

where ψ_{r} is the rotor flux and T_{e} is the electromechanical torque, p is the number of poles, K_1 and K_2 are the gains of the flux flow path and torque flow path, respectively. In IFOC, the $\psi_{\mathrm{qr}} = 0$ and $\psi_{\mathrm{dr}} = \psi_{\mathrm{r}}$. The gain K_3 is used to generate the ω_{sl} following Eq. (4) which in turn helps to generate a unit vector for axis transformation as shown in Eq. (5)

$$K_3^{*} = \omega_{\mathrm{sl}}^{*} = \frac{1}{T_{\mathrm{r}}}\frac{i_{\mathrm{qs}}^{*}}{i_{\mathrm{ds}}^{*}}, K_3 = \omega_{\mathrm{sl}} = \frac{1}{T_{\mathrm{r}}}\frac{i_{\mathrm{qs}}}{i_{\mathrm{ds}}}, T_{\mathrm{r}} = \frac{L_{\mathrm{r}}}{R_{\mathrm{r}}} \tag{4}$$

$$\theta_s \triangleq \int \omega_s dt \tag{5}$$

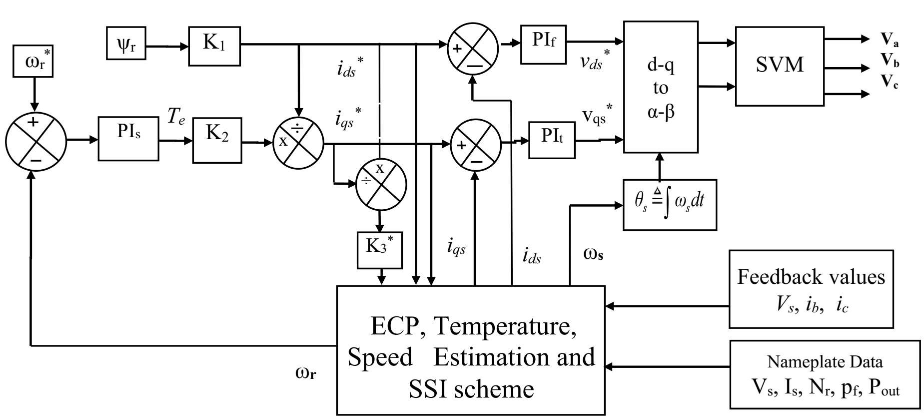

Fig. 3 Schematic of IFOC controller

As seen in Fig. 3, three PI controllers are used, in the torque and flux flow path along with i_{ds}^{*} and i_{qs}^{*} signals. The torque control can be achieved from speed error since the developed electromagnetic torque affects the speed dynamically. Applying PI controller into the error signal between reference and measured or calculated speed and current. The PI_s are the representation of the PI controller in the torque flow path.

$$T_e \triangleq \left(K_{pIs} + \frac{K_{iIs}}{s}\right)(\omega_r^* - \omega_r),\ i_{qs}^* = \frac{\left(K_{pIs} + \frac{K_{iIs}}{s}\right)(\omega_r^* - \omega_r)K_2}{i_{ds}^*} \tag{6}$$

The errors between the actual and reference values of i_{ds} and i_{qs} are fed to the respective PI controllers (PI_f and PI_T) to generate equivalent d-q axis voltages (v_{ds}^{*}, v_{qs}^{*}).

$$v_{ds}^* = \left(K_{pIf} + \frac{K_{iIf}}{s}\right)(i_{ds}^* - i_{ds}),\ v_{qs}^* = \left(K_{pIt} + \frac{K_{iIt}}{s}\right)\left(i_{qs}^* - i_{qs}\right) \tag{7}$$

The flux ψ_r is estimated with the V_s and ω_r from the nameplate data before the start of the motor and remains almost constant during running for which i_{ds} also remain constant. After transformation to v_α and v_β, the v_{svm} is generated for the SVM to produce PWM pulses for the inverter [1]. The v_{svm} and its inclination angle α [1, 2] are calculated as

$$v_{svm} = \sqrt{v_\alpha^2 + v_\beta^2},\ \alpha = \tan^{-1}\frac{V_{qs}}{V_{ds}} = \tan^{-1}\frac{v_\alpha}{v_\beta} \tag{8}$$

Using Eq. (8) the switching instances of the space vector modulation (SVM) are determined as

$$t_1 \triangleq \frac{2\sqrt{3}MT_c \sin\left(\frac{\pi}{3} - \alpha\right)}{\pi},\ t_2 \triangleq \frac{2\sqrt{3}MT_c \sin(\alpha)}{\pi},\quad \text{and}\quad t_0, t_7 \triangleq (T_c - t_1 - t_2) \tag{9}$$

where the modulation index M is given by

$$M = \frac{v_{svm}}{2v_{dc}/\pi} \tag{10}$$

where $T_c = T_{pwm}/2$, and T_{pwm}. The instantaneous phase voltage is shown in Eq. (11) by time averaging of the space vectors during one switching period for the sector.

$$\begin{aligned} V_{an} &= \frac{V_s}{2T_c}\left(\frac{-t_0}{2} + t_1 + t_2 + \frac{t_0}{2}\right),\ V_{bn} = \frac{V_s}{2T_c}\left(\frac{-t_0}{2} - t_1 + t_2 + \frac{t_0}{2}\right), \\ V_{cn} &= \frac{V_s}{2T_c}\left(\frac{-t_0}{2} - t_1 - t_2 + \frac{t_0}{2}\right) \end{aligned} \tag{11}$$

where $T_c = T_{pwm}/2$. It is evident from the above equations that the performance of the IFOC controller is primarily dependent on the equivalent parameters of the IM as well as the gains of the PI controllers. Thus evaluation of equivalent parameters of IM before

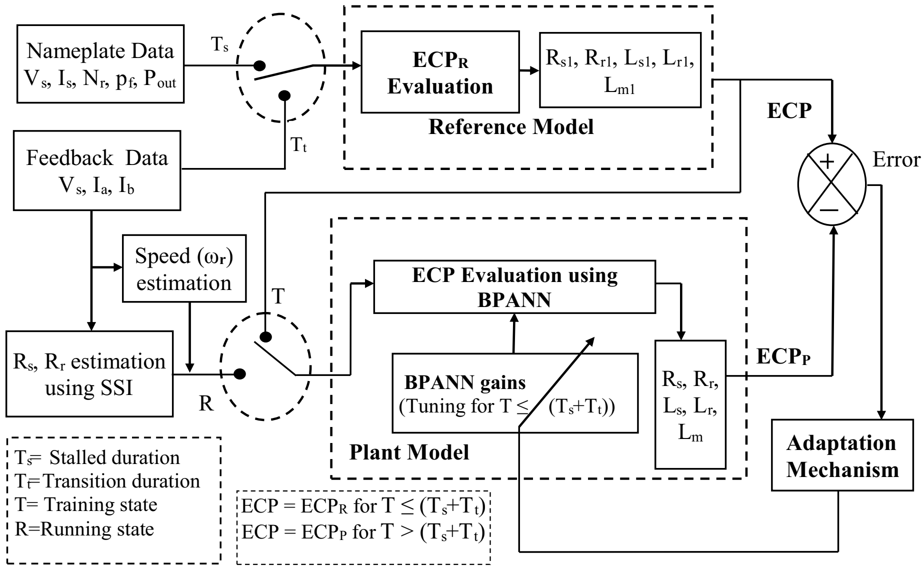

Fig. 4 MRAS scheme for ECPs estimation

starting, during the transition phase as well as during running is essential. Generally, no load and blocked rotor tests of IM are performed to estimate its equivalent parameters. But with our scheme, these tests are avoided as ECPs are evaluated using the proposed MRAS model during the stalled, transition, and running conditions.

Model reference adaptive system for ECPs estimation

To implement the IFOC scheme for the drive, the accurate estimation of the required ECPs is the most challenging task as these ECPs get changed with the running conditions of the motor.

The ECPs depend mostly on the slip, supply frequency, loading, and inside temperature of the motor, the accurate measurement of which are very much essential to get better control performance of the IFOC. Accordingly, an MRAS model [5, 7] for ECPs estimation is developed as shown in Fig. 4. In the form of BPANN, the Reference model and BPANN-based plant model are the two basic building blocks of the controller.

Formulation for reference model M_R

This model is used to generate ECP_R set, i.e. the reference values of ECPs namely R_{s1}, R_{r1}, L_{m1}, L_{s1}, L_{r1} during the pre-start and post-start transition period up to the steady-state running condition of the induction motor. This ECP_R set is utilized to train the gains in the plant model during this entire transition period i.e. till the steady-state running of the motor up to the desired speed is achieved.

ECPR generation before start

The *H-G* diagram method, IEEE 112, and the NEMA specification are used to generate the ECP_R set based on the nameplate data before starting the motor. The stator voltage V_s, stator current I_s (I_a, I_b), rotor speed N_r, input power factor p_f, and output power P_{out} are the nameplate data to be provided. The *H-G* diagram is represented by an operating circle in the complex plane to analyze the power consumption scenario of an IM. The *G* and *H* functions [27] are having the dimension of inductance to represent the active and reactive power consumption status, respectively. The G function is directly related to developed torque and the H function is concerned with the magnetizing flux. The per-phase equivalent circuit impedance of Eq. (1) is modified by ignoring R_c and is expressed as in Eq. (12). The ECP_R set is evaluated using the equations derived as follows:

$$Z_{\mathrm{eqR}} = \frac{V_{\mathrm{s}}}{I_{\mathrm{s}}} = R_{\mathrm{s}} + \omega_{\mathrm{s}} G(\omega_{\mathrm{sl}}) + j\omega_{\mathrm{s}} H(\omega_{\mathrm{sl}}) \tag{12}$$

Following the construction method of the H-G diagram, the operating points on the diagram are a function of slip ω_{sl} and can be expressed as

$$G(\omega_{sl}) = \frac{L_{m1}\omega_{sl}R_{r1}}{R_{r1}^2 + L_{r1}^2\omega_{sl}^2}L_{m1} \tag{13}$$

$$H(\omega_{sl}) = L_{s1} - \frac{L_{m1}^2\omega_{sl}^2}{R_{r1}^2 + L_{r1}^2\omega_{sl}^2}L_{r1} \tag{14}$$

Since $G(\omega_{sl})$ and $H(\omega_{sl})$ represent active and reactive power consumption, their locus describes a circle in the so-called H-G plane for the variation in load or even change in the ECPs for any other reasons [17]. This circle is graduated with the ω_{sl} increasing from the purely synchronous point H_0 to its point H_∞, from which stator inductance L_s and the total leakage coefficient σ can be derived using Eq. (15)

$$L_{\mathrm{s}} = H_0 = \frac{\phi_{\mathrm{nl}}}{I_{\mathrm{nl}}} = \frac{V_{\mathrm{s}}}{I_{\mathrm{nl}}\omega_{\mathrm{s}}}, \ \sigma = \frac{H_\infty}{H_0} \tag{15}$$

where the current I_{nl} can be evaluated from the nameplate data and NEMA specification without performing the real hardware test. It is assumed that σ is quite small for which $H_\infty \approx 0$, circle diameters become directly a function of the stator flux ψ_s as shown in Eq. (16). The H-G diagram identifies the parameters in the (α, β) reference frame. The *P* and *Q* power components are estimated from the dot and cross product of the V_s and I_s vectors in the (α, β) reference frame using Clarke Transformation. The values of *P* and *Q* are obtained as

$$\left.\begin{aligned} P &= V_{\mathrm{s}(\alpha,\beta)} \cdot I_{\mathrm{s}(\alpha,\beta)} = V_{\mathrm{s}\alpha}I_{\mathrm{s}\alpha} - V_{\mathrm{s}\beta}I_{\mathrm{s}\beta} \\ Q &= V_{\mathrm{s}(\alpha,\beta)} \times I_{\mathrm{s}(\alpha,\beta)} = V_{\mathrm{s}\alpha}I_{\mathrm{s}\beta} - V_{\mathrm{s}\beta}I_{\mathrm{s}\alpha} \end{aligned}\right\} \tag{16}$$

The values of $G(\omega_{sl})$ and $H(\omega_{sl})$ at any instantaneous point i can also be calculated from given P and Q as

$$G_i = G(\omega_{sl}) = \frac{1}{\omega_s}\left(\frac{P}{I^2_{s(\alpha,\beta)}} - R_s\right) \tag{17}$$

$$H_i = H(\omega_{sl}) = \frac{Q_i}{\omega_s I^2_{s(\alpha,\beta)}} \tag{18}$$

$$R_{r1} = \frac{\frac{P}{I^2_{s(\alpha,\beta)}}}{\left(1 - \frac{H_i}{H_0} + k\right)}, R_{s1} = kR_{r1} \tag{19}$$

where k is obtained from NEMA guidelines. The stator and rotor resistance R_{s1} and R_{r1} and rotor time constant τ_r can then be estimated from $G(i)$ and $H(i)$ as,

$$\tau_r = \frac{L_{r1}}{R_{r1}} = \frac{H_0 - H_i}{\omega_{sl} G_i} \text{ and thus } L_{r1} = L_{s1} \tag{20}$$

Thus the value of rotor inductance L_{r1} can be estimated from τ_r and R_{r1}. The mutual inductance can thus be evaluated as

$$L_{ml} = \sqrt{\left(\frac{(L_{s1} - H_i)(R^2_{r1} + L^2_{r1}\omega^2_{sl})}{L_{r1}\omega^2_{sl}}\right)} \tag{21}$$

The gain parameters of IFOC K_1, K_2, and K_3 as shown in Eqs. (2)–(4) are evaluated using the ECP_R set from the nameplate data before starting.

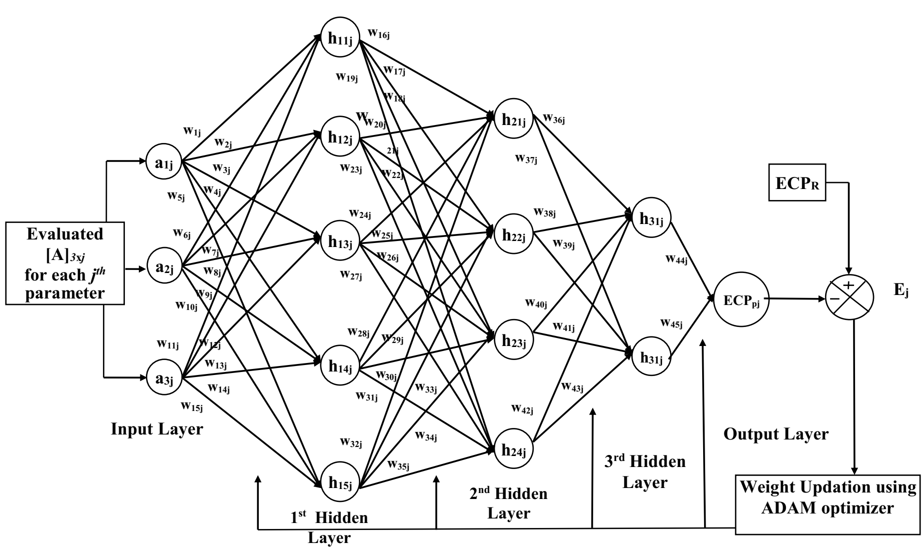

Fig. 5 Plant Model for ECPs estimation

ECPR generation during the transition phase

It is evident from Eq. (2) that the value of ψ_r is dependent on the mutual inductance. But the mutual inductance varies on variations in resistances and both of them vary due to variations in motor temperature during the running condition. This in turn causes a change in i_{ds} and IFOC logic accordingly. Thus though the H-G diagram method is efficient enough for estimating the ECPs during the pre-start condition, its use is not suggested during the running condition. Accordingly, during the transition phase, the feedback values like V_s, I_a, and I_b are provided as input to the reference model on basis of which the ECP_R is generated using equations are (16)–(21) to tune the plant model ECP_p. The value of $I_{s\alpha\beta}$ (i_α,i_β) and the $V_{s\alpha\beta}$ (V_α, V_β) are evaluated using Clarke transformation as shown in figure vii7.

Formulation for plant model M_P

The estimated ECP_R set, using the above-described method, provides accurate results so long the operating conditions, i.e. load demand, slip, temperature, supply frequency remain unaltered. But, as the values of R_{s1}, ω_{sl} varies with change in motor temperature and slip, the estimated ECP_R set, L_m value in particular, from the H-G method produces an erroneous result. This needs a switchover of the ECPs estimation from the reference model to the plant model during the running condition of the motor. The plant model is built based on the backpropagation principle where ANN with an input layer of three neurons and three hidden layers of five, four, and two neurons respectively, and one output neuron model (3-5-4-2-1) is used in its forward path as shown in Fig. 5. The value of each of the ECPs, i.e. R_s, R_r, L_r, L_s, and L_m, have been evaluated accurately during steady state. For working of BPANN, an input matrix $[A]_{3\times5}$ is constituted where each row contains three values of one of the parameters and each column represents each of the parameters of R_s, R_r, L_r, L_s, and L_m. Out of the three values of each row *j*, one value (a_j) is calculated by using the respective equations from (22) to (24) and the other two values are estimated considering a deviation range of±€. This creates a set of values like [a_j−ε, a_j, a_j+ε] for each row *j* of $[A]_{3\times5}$ and is treated as the input neurons for the ANN module to estimate the parameter corresponding to that row *j*. As *j* can vary from 1 to 5 to represent R_s, R_r, L_r, L_s, and L_m, respectively, the ANN structure is to be utilized four times to estimate all the ECPs in a one-time step. The entire operation of the plant model can be divided into two subparts—namely (i) starting, i.e. start of the motor from standstill to the set speed achievement and (ii) running conditions of the motor. The functioning of ECPs under these conditions is described below.

ECPs evaluation during the transition period

Before start, the ECP_R values are utilized for input matrix $[A]_{3\times5}$ and the weight updation procedure begins offline so that the overall time of convergence can be minimized. After the offline training is done the IM is started with the parameters obtained from M_R. During this period, ECPs copy the values of ECP_R to generate the triggering pulses following IFOC schemes. It is considered that the value of L_s and L_r are assumed to be the same for small to medium motors whereas the ratio between these two parameters can be taken as per NEMA specifications for larger motors for their evaluation. The value of R_s and R_r is estimated using (22) where v_{ssi} and i_{ssi} are the voltage and current signals derived from the SSI method as illustrated in "Estimation of R_s using small signal injection method" section.

$$R_{\mathrm{s}} = \frac{v_{\mathrm{ssi}}}{i_{\mathrm{ssi}}}, R_{\mathrm{r}} = R_{\mathrm{s}}/k \tag{22}$$

Therefore the inductances can be evaluated as

$$L_{\mathrm{s}} + L_{\mathrm{r}} = \frac{1}{2\pi f}\sqrt{\left(\frac{V_{\mathrm{s}}}{I_{\mathrm{r}}}\right)^2 - \left(R_{\mathrm{s}} + \frac{R_{\mathrm{r}}}{s}\right)^2} \tag{23}$$

where slip s is changing with the estimated speed

$$L_{\mathrm{m}} = \frac{1}{2\pi f}\frac{P_{\mathrm{nl}}}{V_{\mathrm{s}} I_{\mathrm{nl}}\sqrt{1 - p_{\mathrm{fnl}}^2}} \tag{24}$$

Considering the inputs of each BPANN topology as

$$a_{j1} = a_j - \varepsilon,\ a_{j2} = a_j,\ a_{j2} = a_j + \varepsilon \tag{25}$$

three such inputs for each j are mapped to the four neurons of the first hidden layer by their corresponding weight factor w. The selection of the weights is done in a random manner such that the neurons of this layer are initialized as in Eq. (26)

$$\begin{bmatrix} h_{11j} \\ h_{12j} \\ h_{13j} \\ h_{14j} \\ h_{15j} \end{bmatrix} = \begin{bmatrix} w_{1j} & w_{6j} & w_{11j} \\ w_{2j} & w_{7j} & w_{12j} \\ w_{3j} & w_{8j} & w_{13j} \\ w_{4j} & w_{9j} & w_{14j} \\ w_{5j} & w_{10j} & w_{15j} \end{bmatrix} \begin{bmatrix} a_{j1} \\ a_{j2} \\ a_{j3} \end{bmatrix} \tag{26}$$

The BPANN structure is designed in such a way that the vanishing gradient and exploding gradient problems are minimum. For simplicity, the number of the hidden layer is considered to be two where Leaky Relu and Adam activation function is used for optimization. But in some work [30, 31] use of three hidden layers has also been considered to improve accuracy. The use of three hidden layers poses the problems like: (i) increase in network complexity, (ii) increase in convergence time, as well as the number of iterations to converge, (iii), increases the processor's computational overhead, and accordingly, high power processors are required for its implementation. Whereas with the use of two hidden layers, these problems are very less and the system with two hidden layers can easily be implemented with a low-power processor. But considering the accuracy aspects for the evaluation of ECPs of IM, three hidden layer system control structure is considered in this work. The activation function used here is Leaky Relu which is defined as $S_{ir}(h) = h_{ir}$ for $h_{ir} \geq 0$ or $S_{ir}(h) = 0.01h_{ir}$ for $h_{ir} < 0$ where i represents the number of hidden layers and r represents the number of neurons in that particular hidden layer. For this design, i and r maybe 1 to 2 and 1 to 4, respectively. The second hidden layer neurons are represented similarly as given by

$$\begin{bmatrix} h_{21j} \\ h_{22j} \\ h_{23j} \\ h_{24j} \end{bmatrix} = \begin{bmatrix} w_{16j} & w_{20j} & w_{24j} & w_{28j} & w_{32j} \\ w_{17j} & w_{21j} & w_{25j} & w_{29j} & w_{33j} \\ w_{18j} & w_{22j} & w_{26j} & w_{30j} & w_{34j} \\ w_{19j} & w_{23j} & w_{27j} & w_{31j} & w_{35j} \end{bmatrix} \begin{bmatrix} s_{11j} \\ s_{12j} \\ s_{13j} \\ s_{14j} \\ s_{15j} \end{bmatrix} \tag{27}$$

$$\begin{bmatrix} h_{31j} \\ h_{32j} \end{bmatrix} = \begin{bmatrix} w_{36j} & w_{38j} & w_{40j} & w_{42j} \\ w_{37j} & w_{39j} & w_{41j} & w_{43j} \end{bmatrix} \begin{bmatrix} s_{21j} \\ s_{22j} \\ s_{23j} \\ s_{24j} \end{bmatrix} \tag{28}$$

The output of the ECP_{pj} is expressed as

$$ECP_{pj} = \begin{bmatrix} w_{44j} & w_{45j} \end{bmatrix} \begin{bmatrix} s_{31j} \\ s_{32j} \end{bmatrix} \tag{29}$$

Besides, the BPANN algorithm is designed in such a way that the weight factors are trained during the speed transient period and/or starting period of the motor while these periods are identified till the desired set speed is achieved from the very start i.e. stopped or stalled condition of the motor.

For the training purposes, each of the output parameters from M_P is compared with the respective reference parameters coming out from M_R i.e. the error between the parameters of the M_R and M_P are $E_j = (ECP_{Rj}\text{-}ECP_{Pj})$ are evaluated such that The loss or error functions are then generated following Eqs. (35) which are minimized using Adam rule to recalculate the weights in backpropagation manner,

$$b_j = \frac{1}{2}E_j^2, j = [R_s = ECP_{Rs}, R_r = ECP_{Rr}, L_s = ECP_{Ls}, L_m = ECP_{Lm}] \tag{30}$$

where b_j is the loss function for each of the jth parameters. Thus the weight updation process or the training process continues until the difference between the output of all the elements of M_R and M_P will be less than or equal to the tolerance limit δ,

$$E_j = ECP_R - ECP_{Pj} = \pm\delta \tag{31}$$

The basic weight updation rule as stated in the gradient descend (GD) method is expressed as in Eq. (32). This weight updation method is modified as per the ADAM rule as described in Eq. (35–38). This ADAM rule is a combined form of the Adagrad and RMSProp adaptive GD method, the details of which are explained in reference (25), and hence the description is not included in this paper.

$$w_{(n+1)} = w_{(n)} - \eta\frac{\partial E}{\partial w_n}, g_n = \frac{\partial E}{\partial w_n} \tag{32}$$

$$w_{(n+1)} = w_{(n)} - \frac{\eta}{\sqrt{\gamma + r_n^*}} \times m_n^* \tag{33}$$

where m_n is the momentum term and the value of m_n and r_n is given by

$$m_n = \beta_n \times (m_{n-1} - 1) + (1 - \beta_1) \times g_n, g_n = \frac{\partial E}{\partial w_n} \tag{34}$$

$$r_n^* = \beta_n \times (r_{n-1} - 1) + (1 - \beta_2) \times g_n^2 \tag{35}$$

and

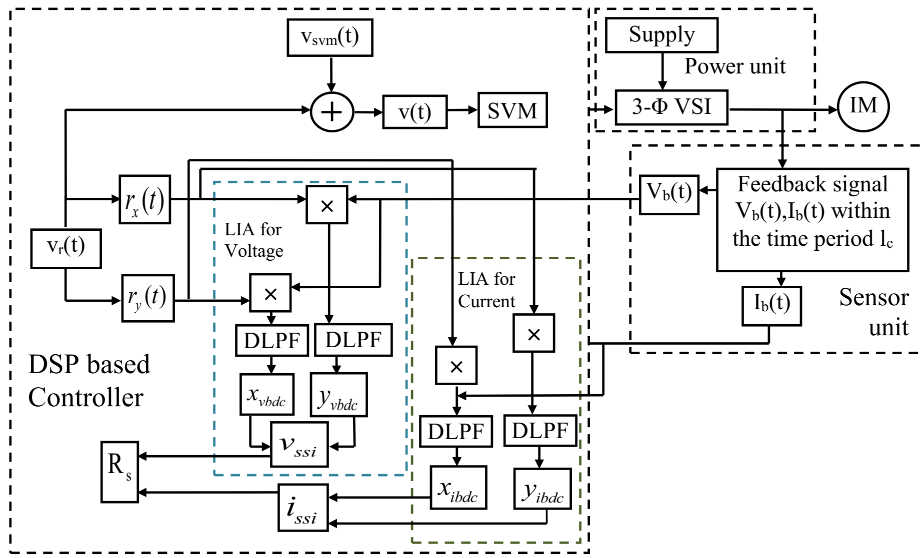

Fig. 6 Schematic of Signal injection method

$$m_n^* = \frac{m_n}{1-\beta_1^n}, r_n^* = \frac{r_n}{1-\beta_2^n}, \beta_1 = 0.9, \beta_2 = 0.999 \tag{36}$$

The BPANN gain tuning procedure continues till the weight updating rule is satisfied, the duration of which is well within the starting transition period of the motor.

ECPs evaluation during running

Once the training period is over, the ECPs estimation is started with the plant model by making a switch over to the selection of input towards sampled feedback of (V_s, $I_s(I_a, I_b)$). The parameters are calculated using Eqs. (22)–(24) to form the input matrix of BPANN and then this $[A]_{3\times5}$ is used to evaluate ECP_P. The values of K_1, K_2, and K_3 are also evaluated following Eq. (37), and all the IFOC d-q voltage, current, flux, slip frequency, etc., are calculated using Eq. (2)–(11).

$$K_1 = \frac{1}{ECP_{L_m}}, K_2 = \frac{4ECP_{L_r}}{3pECP_{L_m^2}}, K_3 = \frac{ECP_{R_r}}{ECP_{L_r}} \tag{37}$$

Stator resistance and speed estimation

Estimation of R_s using small signal injection method

The R_s measurement method is based on the injection of a very low-frequency, low amplitude lock-in signal to the stator along with the three-phase supply fed to the motor using the converter. A basic lock-in system consists of a lock-in signal generator, an amplifier, a PSD, and a low pass filter, the schematic diagram of which is shown in Fig. 6. All the constituent blocks of Fig. 6 are grouped into DSP-based lock-in signal generators with LIA for voltage and LIA for current, sensor unit, and power unit blocks for a better understanding of their working. The DSP-generated lock-in signal of very low amplitude is passed through the stator along with the stator voltage after their necessary modulation to produce a lock-in stator current depending on the stator resistance. This lock-in current is amplified to a level adequate for the PSD in the sensor unit and is then passed through an LPF to extract the noise-free return current signal. The stator resistance is estimated during running conditions with the ratio of the injected lock-in voltage and the return current signal. The amplitude of lock-in voltage v_{r} is made so small that it is unable to contribute any impact on the running of the motor while its frequency is made very low so that its inductive effect can be neglected and the return current I_{r} will be limited only by the stator resistance R_{s}. Besides, this kind of infinitesimally small impact is further reduced with the intricacies of intermittent injection of lock-in signals. In its intermittent operation, the lock-in signal is injected for its one-period duration at an interval of nT_{lc} making a duty cycle δ_{lc} such that $\delta_{\mathrm{lc}} = T_{\mathrm{lc}}/nT_{\mathrm{lc}}$ where n is the number of cycles and $T_{\mathrm{lc}} = 1/f_2$ is the period of lock-in signal of frequency f_2. The term $f_3 = 1/nT_{\mathrm{lc}}$ can also be termed as refresh rate for R_{s} estimation. The $v_{\mathrm{svm}}(t)$ is added with a very small ac signal of amplitude $v_{\mathrm{r}}(t)$ and frequency (f_2) to produce a resultant voltage $v(t)$ for δ_{lc} period such that

$$v(t) = v_{\mathrm{svm}}(t) + v_r(t) \;\text{ for }\; 0 \le t \le \delta_{lc} \;\text{ and }\; v(t) = v_{\mathrm{svm}}(t) \text{ else} \tag{38}$$

For detection purposes during δ_{lc} period, the DSP-based processor multiplies the feedback voltage $V_{\mathrm{b}}(t)$ with a modulating signal $r(t)$ having the same amplitude and frequency as that of the $v_{\mathrm{r}}(t)$. The in-phase component of $v_{\mathrm{r}}(t)$ is $r_x(t) = \sin(2\pi f_2 t)$ and quadrature (90° shifted) $r_y(t) = \cos(2\pi f_2 t)$ components which produces $x_{\mathrm{vb}}(t)$ and $y_{\mathrm{vb}}(t)$, respectively, so that

$$x_{\mathrm{vb}}(t) = v_{\mathrm{b}}(t) \times r_x(t), \quad y_{\mathrm{vb}}(t) = v_{\mathrm{b}}(t) \times r_y(t) \tag{39}$$

After this, both the signals are passed through the digital low pass filter to eliminate all the ac components and only the dc component is obtained of both in-phase x_{vbdc} and quadrature component y_{vbdc}. Thus the voltage obtained after filtering is

$$v_{\mathrm{ssi}} = \sqrt{x_{\mathrm{vbdc}}^2 + y_{\mathrm{vbdc}}^2} \tag{40a}$$

The current $i_{\mathrm{b}}(t)$ is also sensed by the Hall sensor which contains the load current, harmonic distortion, and noise component. The $i(t)$ is also multiplied by the same $r(t)$.

$$x_{i\mathrm{b}}(t) = i_{\mathrm{b}}(t) \times r_x(t), \; y_{i\mathrm{b}}(t) = i_{\mathrm{b}}(t) \times r_y(t) \tag{40b}$$

After this, both the signals are passed through the digital low pass filter where the noise, harmonic distortion, and the other ac components get filtered and the only dc component is obtained as $x_{i\mathrm{bdc}}$ and $y_{i\mathrm{bdc}}$. Thus the value of i_{ssi} is given by

$$i_{\mathrm{ssi}} = \sqrt{x_{i\mathrm{bdc}}^2 + y_{i\mathrm{bdc}}^2} \tag{40c}$$

The frequency (f_2), as well as the amplitude of $v_{\mathrm{r}}(t)$, is kept very low so that its contribution to the net flux production is negligibly small such that

$$\left|j \times 2pi \times f_2 \times L_{\mathrm{M}}\right| \leq \left|\frac{R_{\mathrm{r}}}{s} + jL_{\mathrm{r}} \times 2pi \times f_2\right| \tag{41}$$

Thus the stator resistance can thus be computed as follows

$$R_{\mathrm{s}} = \frac{v_{\mathrm{ssi}}}{i_{\mathrm{ssi}}} \tag{42}$$

Thus this method of resistance estimation takes care of the temperature effect of the motor and thus the use of a temperature sensor is avoided. Again if the temperatures of the motor ($T_{(\mathrm{lc}+1)}$ and T_{lc}) are known at two different running conditions, the corresponding resistances can also be evaluated using equation (43) provided the coefficient of expansion λ is known

$$R_{\mathrm{slc}+1} = R_{\mathrm{slc}}(1 + \lambda \Delta T_{\mathrm{lc}}) \quad \text{where} \quad \Delta T_{\mathrm{lc}} = T_{\mathrm{lc}+1} - T_{\mathrm{lc}} \tag{43}$$

where $R_{\mathrm{s(lc+1)}}$ and $t_{\mathrm{lc}+1}$ represent the current value of the resistance and temperature, and R_{slc} and t_{lc} denote the precious value, respectively.

Sensorless speed estimation scheme

The performance of the IFOC scheme depends on the variation of temperature which varies due to environmental changes, the presence of harmonics, and overloading as both the stator resistance R_{s} and the rotor resistance R_{r} vary with it. Fluctuations in the speed may occur due to a change in load, change in the time constant due to temperature rise. For a variation of R_{r}, the time constant ($\tau_{\mathrm{r}} = L_{\mathrm{r}}/R_{\mathrm{r}}$) varies inversely. An increase in temperature in general increases the rotor and stator copper losses P_{rcl}, P_{scl} for which the total loss P_{loss} increases. Thus if the supply voltage V_{s} and the output power (P_{out}) remain constant, IM will draw more power from the input for which the motor efficiency will reduce and the stator and rotor currents (I_{s}, I_{r}) will also increase. In normal operating conditions, as the motor starts picking up with the speed the torque T_{e} becomes maximum at slip s_{m} before coming to the operating point following Eq. (45)

$$\omega_{\mathrm{r}} = \omega_{\mathrm{s}}\left(1 - \frac{s_{\mathrm{m}} T_{\mathrm{e}}}{2T_{\mathrm{em}}}\right), \; s_{\mathrm{m}} = \frac{R_{\mathrm{r}}}{L_{\mathrm{s}} + L_{\mathrm{r}}} \tag{44}$$

Thus the rotor speed varies with ECPs variation. At steady state, the d-q axis voltages can be expressed by Eqs. (45) and (46) considering constant flux by neglecting the rate of change of flux.

$$v_{\mathrm{ds}}^{*} = R_{\mathrm{s}} i_{\mathrm{ds}}^{*} - \omega_{\mathrm{s}} \sigma L_{\mathrm{s}} i_{\mathrm{qs}}^{*}, \; \sigma_1 = 1 - \frac{L_{\mathrm{m}}^2}{L_{\mathrm{s}} L_{\mathrm{r}}} \tag{45}$$

$$v_{\mathrm{qs}}^{*} = R_{\mathrm{s}} i_{\mathrm{qs}}^{*} + \omega_{\mathrm{s}} \sigma_1 L_{\mathrm{s}} i_{\mathrm{ds}}^{*} \tag{46}$$

The reactive power can be expressed as in Eq. (47)

$$Q_1 = v_{\mathrm{qs}} i_{\mathrm{ds}} - v_{\mathrm{ds}} i_{\mathrm{qs}} \tag{47}$$

By substituting the value of $v_{ds}{}^{*}$ and $v_{qs}{}^{*}$ in the above equation, the reference value of the reactive power is

$$Q_1^* = \omega_s(L_s i_{ds}^{*2} + \sigma_1 L_s i_{qs}^{*2}) \tag{48}$$

assuming negligibly small measurement error, the reference values of ($v_{ds}{}^{*}$, $v_{qs}{}^{*}$, $i_{ds}{}^{*}$, $i_{qs}{}^{*}$) must be equal to the measured values (v_{ds}, v_{qs}, i_{ds}, i_{qs}), and hence the reactive power evaluated with reference values must be equal to the actual value. Thus by equating (47) and (48)

$$\omega_s = \frac{v_{qs} i_{ds} - v_{ds} i_{qs}}{(L_s i_{ds}^{*2} + \sigma_1 L_s i_{qs}^{*2})} \tag{49}$$

Accordingly, the shaft speed is estimated by

$$\omega_r = \omega_s - \omega_{sl}, \quad \text{where } \omega_{sl} = \left(K_{psl} + \frac{K_{isl}}{s}\right)(K_3^* - K_3) \tag{50}$$

where $\omega_{sl}{}^{*}$ and ω_{sl} can be expressed as in Eq. (4). Before start, the ω_r is estimated by

$$\omega_r = \omega_s - \omega_{sl}^* \tag{51}$$

To ensure accurate estimation of the ω_{sl}, a PI controller with gain $k_{p\omega sl}$, $k_{i\omega sl}$ is introduced as in Eq. (51) Substituting this ω_{sl} in Eq. (51) the expression modified shaft speed expression will be.

$$\omega_r = \omega_s - \left(K_{psl} + \frac{K_{isl}}{s}\right)(K_3^* - K_3) \tag{52}$$

With this accurate performance speed estimation is achieved. The PI controller here is tuned using the Z-N method. The schematic of the speed estimation method is shown in Fig. 7.

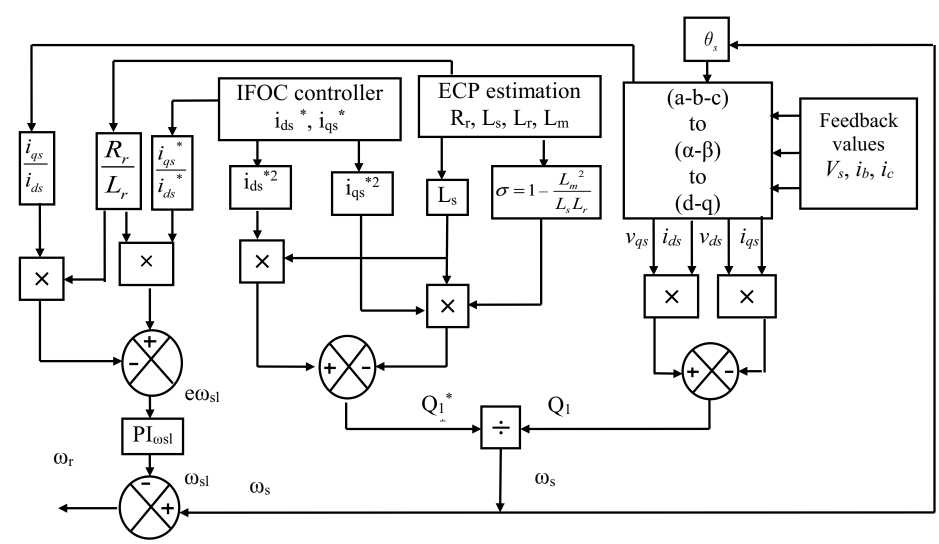

Fig. 7 Schematic of Speed estimation method

Flowchart for the proposed BPANN based optimization method

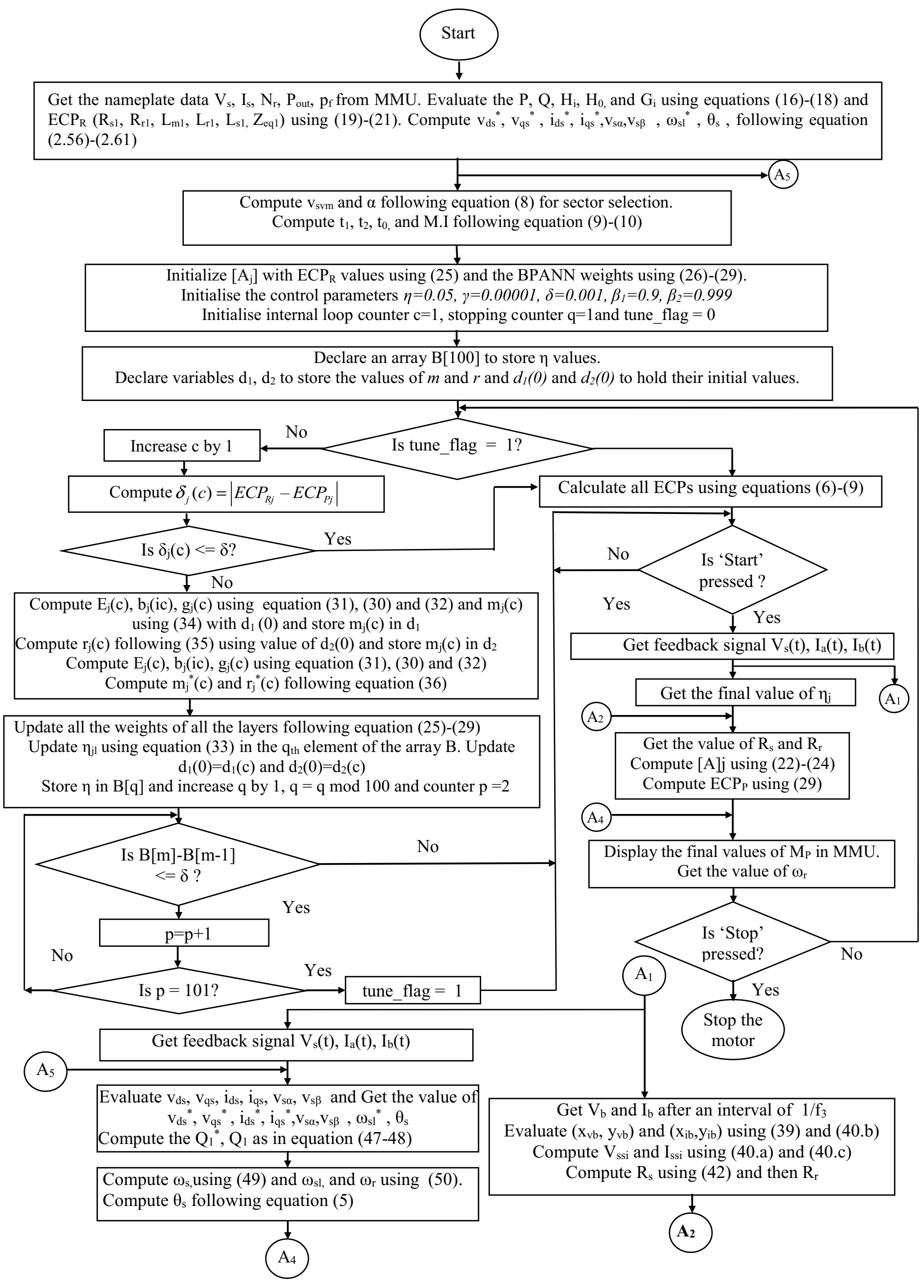

Experimentation

The viability of the proposed controller development based on the Adam technique is tested in two stages—(i) in the first stage, the entire scheme is simulated using MATLAB/Simulink environment while (ii) the simulated development is tested with actual hardware implementation as well a customized graphical user interface (GUI) development for parameter monitoring purposes, all of which are described as follows.

Table 1 ECPs evaluation using system models and physical tests

ECPs	ECPs evaluated from models				%Errors			
	PT test	M_R (with H-G diagram)	M_P (with GD optimizer	M_P (with ADAM optimizer	(PT-M_R)	(PT-M_P) with GD	(PT-M_P) with ADAM	Paper [20]
R_S in Ω	1.85	1.85002	1.8501	1.85002	−0.001	−0.0054	0.001	0.0002
R_R in Ω	1.84	1.840	1.83997	1.84	−0.00	0.0016	0.00	0.0001
X_S/X_R in Ω	53.38	53.3771	53.37742	53.40	0.0054	0.0048	0.0112	0.0396
L_S or L_R in mH	170	169.94	170.22	170.02	0.0054	0.0048	0.0112	0.0396
L_m in mH	160	159.952	159.968	160.01	0.03	0.02	0.0062	0.0086

Table 2 ECPs evaluation using 2 and 3 hidden layers

	PT	ECPs with two hidden layers				ECPs with three hidden layers			
		GD	AD	Accuracy with GD (%)	Accuracy with AD (%)	GD	Adam	Accuracy with GD (%)	Accuracy with AD (%)
R_s	1.85	1.833	1.846	99.08	99.7	1.8501	1.85002	100	100
R_r	1.84	1.8239	1.836	99.125	99.78	1.83997	1.84	99.99	100
L_s/L_r	170	167.7	168.12	98.64	98.89	170.22	170.02	100.1	100.011
L_m	160	156.95	158.21	98.093	98.88	159.968	160.01	99.98	100.0625
τ_r	0.09239	0.09194	0.0915	99.51	99.03	0.092515	0.09240	100.135	100.01
ω_r	147.0462	147.998	146.95	100.64	99.93	147.06	147.048	100.009	99.999
ω_{sl}	9.9538	10.002	10.05	100.48	100.966	9.94	9.952	99.86	99.98

Simulation results

Case 1: Avoidance of physical tests

The parameters of an IM are simulated using both GD and Adam algorithms based on the nameplate data viz. 3.3 kW, 3-ϕ, 415 V, 50 Hz, 6.9A, 1415 rpm and pf = 0.8. For validation purposes, the equivalent circuit parameters of the motor are evaluated from conventional physical no-load and blocked rotor tests (PT). The parameters estimated from PT, M_R, and M_P are presented in Table 1 along with the percentage error of ECPs with that of paper [12] for comparison purposes. It is evident from Table 1 that the errors are very similar between different methods suggesting the need of performing PT can be avoided.

The ECPs evaluated in Table 1 is based on the BPANN with three hidden layer structure of the plant model as shown in Fig. 5. But for simplicity in implementation purposes, two hidden layer structure is widely used. Thus to make a comparison in achieved accuracy the experiment is also performed with two hidden layers and the result of both two and three are tabulated in Table 2. It is evident from this Table 2 that betterment in accuracy for almost all of the parameters is achieved with a three-layer structure.

Case 2: Tracking performance

The performances of the drive like its speed response at a constant load torque as well as its sudden change are simulated and shown in Figs. 8 and 9 respectively during the

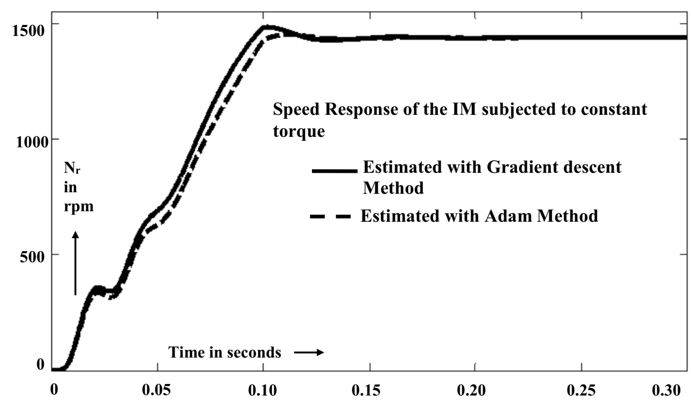

Fig. 8 Speed Response of IFOC VSI-IM drive with constant load

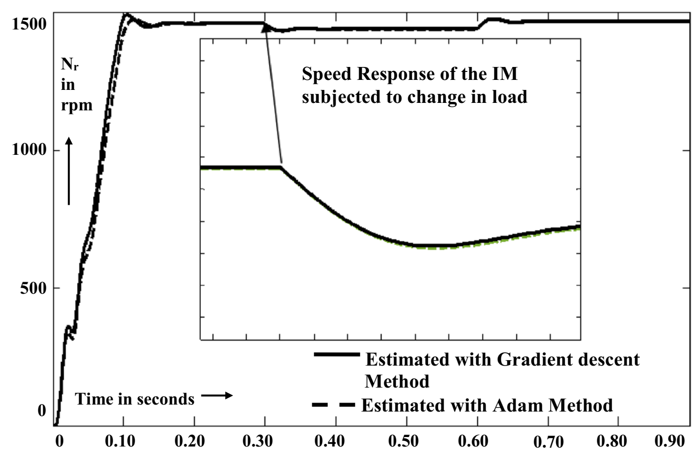

Fig. 9 Speed Response of IFOC VSI-IM drive with a sudden change in load

running condition. It is evident from these Figs. 8 and 9 that the speed responses are similar both in their steady-state and transient conditions for all the BPANN methods.

Case 3: BPANN convergence

The convergence status for BPANN to evaluate the resistance of stator and rotor by using AD and GD methods is shown in Figs. 10 and 11, respectively. Figures 12 and 13 show the convergence graph of reactance L_r/L_s and L_m, respectively. Reaching the steady-state value is considered as the point of convergence. It is evident from these figures that the steady-state value is reached with AD at a faster rate than that with the GD method. This is the reason for which the AD method is adopted in this work.

Case 4: R_s estimation using SSI

The small ac signal of 1 V and 1 Hz is injected along with the A phase supply of V_s of 240 V, 50 Hz, for estimating temperature effect on R_s. The FFT analysis, as shown in Fig. 14, of the A-phase feedback data confirms the presence of this 1 Hz signal injection. As per the proposed design, the only voltage sensor and one of the two current sensors are used in the A phase, the other one is placed either in the B or C phase. The

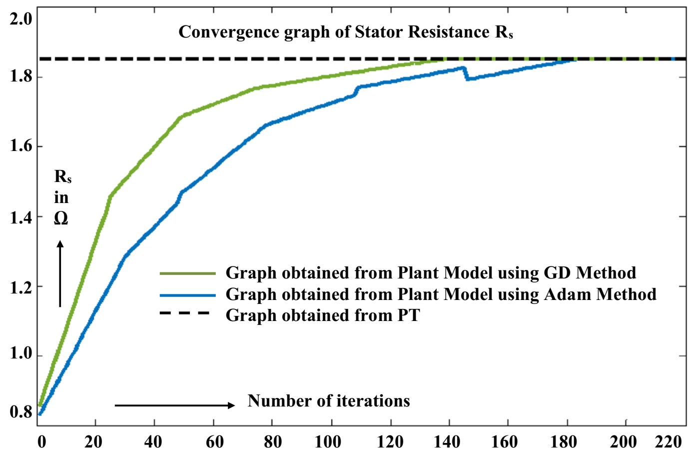

Fig. 10 Convergence of BPANN based estimation of stator resistance R_s

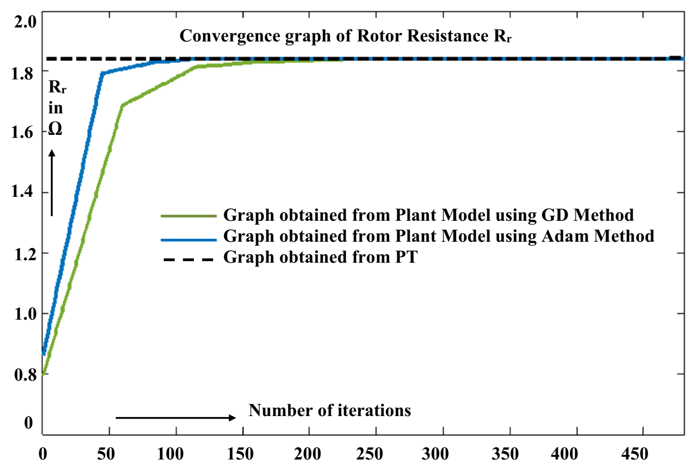

Fig. 11 Convergence of BPANN based estimation of rotor resistance R_r

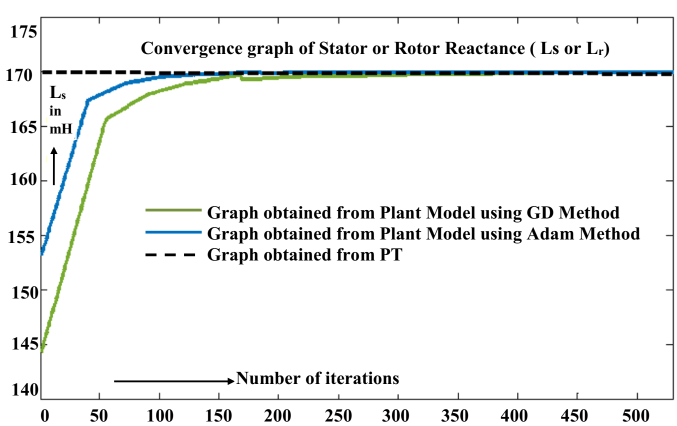

Fig. 12 Convergence of BPANN based estimation of L_s with GD, ADAM methods

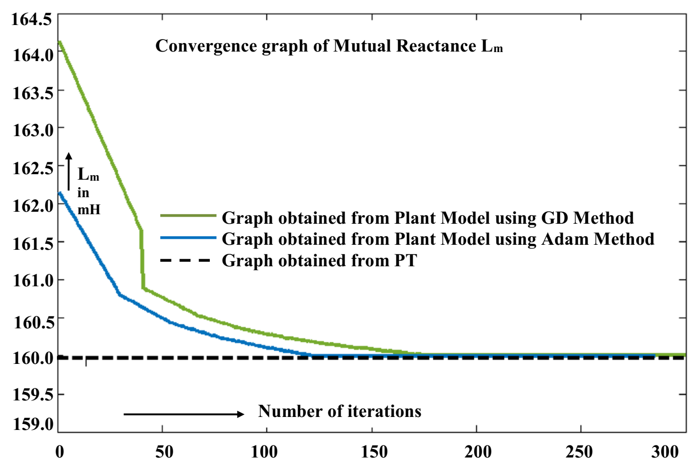

Fig. 13 Convergence of BPANN based estimation of L_m with GD, ADAM methods

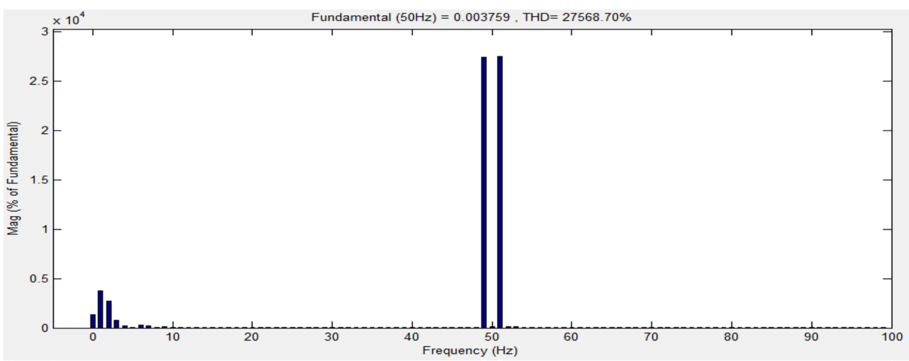

Fig. 14 FFT analysis (presence of 49 and 51 Hz) of received voltage after injection of Lock-in signal

Table 3 R_s estimation using SSI method at various temperatures

At °C	Stator resistance R_s estimated			Effect of R_s Change on other parameters				
	Using SSI	Calculated value	% error	R_r	L_s	τ_r	ω_r	N_r
T*	1.85002	1.85	0.001	1.84	0.1702	0.0925	147.0462	1404.9
$(T+10)$	1.9208	1.9209	0.0052	1.91	0.1702	0.0891	146.711	1401.7
$(T+20)$	1.991	1.9917	0.035	1.98	0.1702	0.0859	146.507	1339.75
(T + 25)	2.027	2.0271	0.0049	2.01	0.1702	0.08467	146.314	1397.91

convolutions of V_a and I_a with v_{rx} and v_{ry} are used to demodulate the lock-in signals while DLPFs are used to extract V_{ssi} and I_{ssi} for the estimation of the R_s. As stated in "Estimation of R_s using small signal injection method" section, this R_s estimation is done only during the δ_{lc} period of the lock-in signal and is refreshed with frequency f_3. The motor temperature proportional values of R_s thus obtained are shown in Table 3 and are assumed to remain constant during the refresh period of the lock-in signal. For this study, δ_{lc} is considered 1 s while the refresh rate is $f_3 = 0.1$ Hz. The evaluated resistances are shown at four different temperatures at T, (T + 10), (T + 20), and (T + 25) where T is the room temperature (25 °C). The same is also estimated using

Table 4 Variation in L_m evaluation using ECP_R and ECP_P with T

Parameters	$ECP_{R(T)}$	$ECP_{R(T+20)}$	Parameters	$ECP_{P(T)}$	$ECP_{P(T+20)}$
R_{s1} in Ω	1.85002	1.991	R_r in Ω	1.85001	1.991
R_{r1} in Ω	1.840	1.9805	R_s in Ω	1.84	1.9805
L_{S1}/L_{r1} in mH	169.94	169.884	L_s/L_r in mH	170.02	170.02
L_{m1} in mH	159.952	**59.79**	L_m in mH	160.01	160.01

The result written in bold is to highlight that at an elevated temperature the reference model based on H-G diagram fails to evaluate the L_m value properly

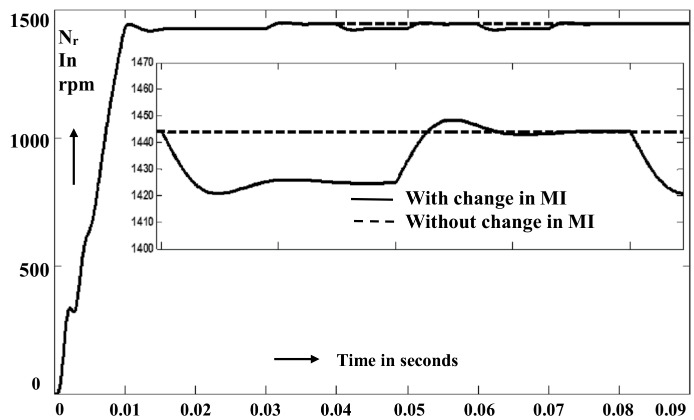

Fig. 15 Speed variation without and with changing MI

the positive temperature coefficient of stator winding λ is the $(3.83 \times 10^{-3}/°C)$ [30] and the % error is evaluated for estimating the efficacy of the proposed SSI.

Case 5: Effect of resistance change

The effect of change in stator resistance on the other parameters of ECPs and speed is also shown in Table 3. It shows how the stator and rotor resistance and rotor time constant τ_R change with temperature. The change in speed indicates that a correction in the firing pulse modulation index is essential otherwise the desired speed can't be achieved. Besides, independent ECPs evaluation using two models at different temperatures is also shown in Table 4. Since Eqs. (17)–(21) and Eqs. (22)–(24) are utilized for ECP_R and ECP_P evaluation, the ECPs values evaluated using these two methods are different for variation in the motor temperature. But considering the running of the motor with fixed load torque, the mutual inductance value should not be changed with temperature. But remarkable change is observed in ECPs evaluation through the M_R model. This suggests ECPs estimation with the H-G diagram method where temperature variation is considered is not suitable during the running of the motor. This also justifies the use of BPANN based plant model in this proposed design.

The changes in stator and rotor resistance and rotor time constant τ_R with temperature change are shown in Table 3. It is observed from the ECPs values in the Table 4 that the modulation index (MI) is needed to be changed to incorporate the effect of temperature changes. If the correction in the MI for this temperature change is not considered, a fluctuation in the developed torque i.e. torque ripple is observed. In other words, there is a fluctuation in the speed as observed in Fig. 15. The reason behind it is that due to the increase in R_s with temperature rise, the developed torque, T_e is reduced, following Eqs. 2 and 6, resulting in a momentary decrease in rotor speed and this error is corrected by the controller and a fluctuation in torque or speed be the result. The no fluctuation in speed is also observed for correction in MI. On the other hand, the change in stator current I_s with and without correction in the MI with the change in R_s is also observed from the Fig. 16. This justifies that a temperature correction is essential to avoid any ripple in the speed or developed torque of the motor.

Experimental results with MMU GUI

Case 6: Hardware controller with MMU system

A DSP-enabled digital signal controller (DSC) featured microcontroller (DSPIC33EP512MC502) with 70 MIPS-based control board is developed for this proposed motor drive system where SVM PWM trigger pulses are generated as per the proposed control algorithm along with the desired feedback signals. These pulses are utilized to control the IGBT-based 3 phase H bridge power hardware through its gate driver system. The IGBT gate driver has also the facility to detect any abnormal operation of the drive for protection purposes. The entire controller logic is embedded within the firmware of this DSC to make it a standalone drive controller. The PWM is designed to operate at 5 kHz (or 200 μs period) and it is observed that the duration for ECPs generation following the above-discussed control algorithm is within 140–180 μs. This proves that the developed drive can be used for online controlling purposes. A snapshot of the developed hardware prototype is shown in Fig. 17. In addition, the values of the internal parameters are sent to a PC through serial communication at a speed of 115.2 kbps for their display in a customized GUI of MMU for monitoring and storage purposes. Some parameters, the nameplate data in particular for starting of the motor and the desired speed are sent to the controller from this GUI. A customized GUI-based MMU using visual basic is designed in such a way that it sends the machine nameplate data to the drive controller once these are fed. The controller then evaluates the equivalent parameters and re-transmits them to the PC for its display in the GUI as shown in Fig. 18. The MMU receives the sample values for motor terminal voltage and current, estimated speed, and measured temperature for their evaluation and display in the GUI. Besides, it is also able to display and store the ECPs of the motor as received from the hardware controller.

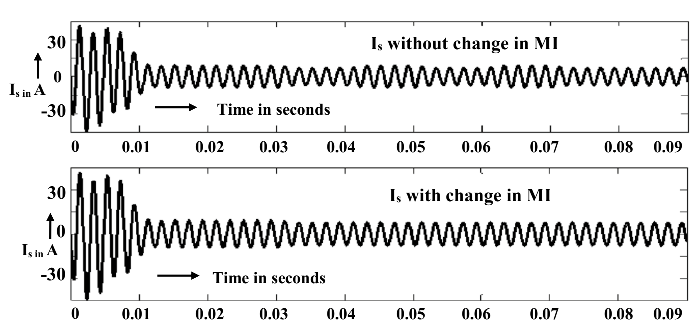

Fig. 16 Current ripple without and with changing MI

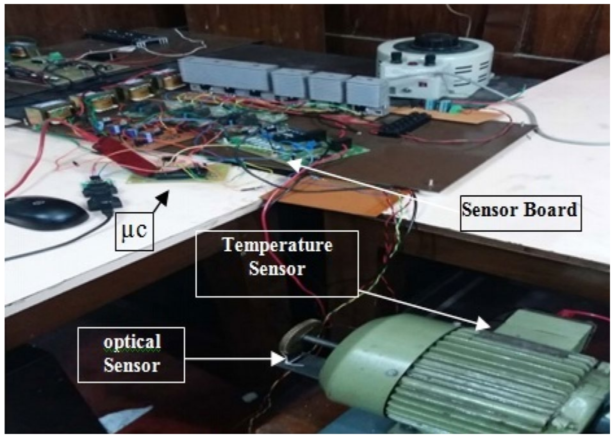

Fig. 17 Hardware prototype model of VSI-IM

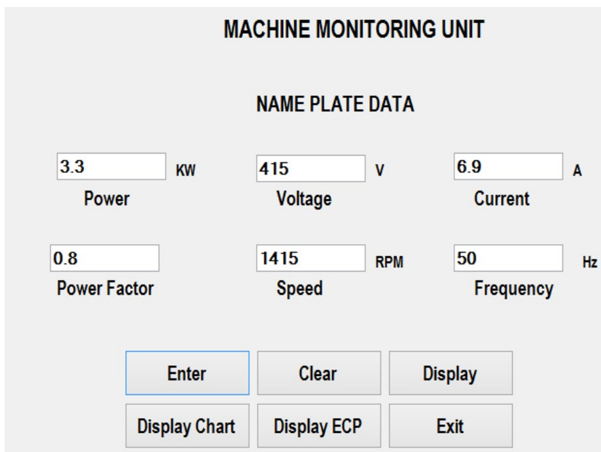

Fig. 18 MMU of VSI-IM showing motor parameters

The microcontroller acquires voltage and current signals through its inbuilt ADC and these data are also transmitted to the PC for monitoring purposes along with other parameter values. The MMU displays these normalized data as shown in Fig. 19 while it's part (a) shows the voltage waveforms and part (b) is for current. The voltage and current data are acquired using voltage (VH1K0T02) and current (HE025T01) sensors respectively. As shown, the lock-in signal to be used to measure R_s is embedded within the acquired voltage or current signals. MMU also displays the estimated ECPs both from M_P and M_R models in its part (c) while its part (d) displays the measured values of voltage and current at an intermediate stage of speed change.

Case 7: ECPs estimation using drive controller

The ECPs values as evaluated by the hardware controller are communicated to the PC at a regular interval of 1 kHz once the training of the BPANN algorithm is completed. Out of all such values, Table 5 shows the ECPs values just after the completion of the training of BPAN along with the other values for comparison purposes. The ECPs data are obtained after taking the average of over 100 observations and accordingly appear very

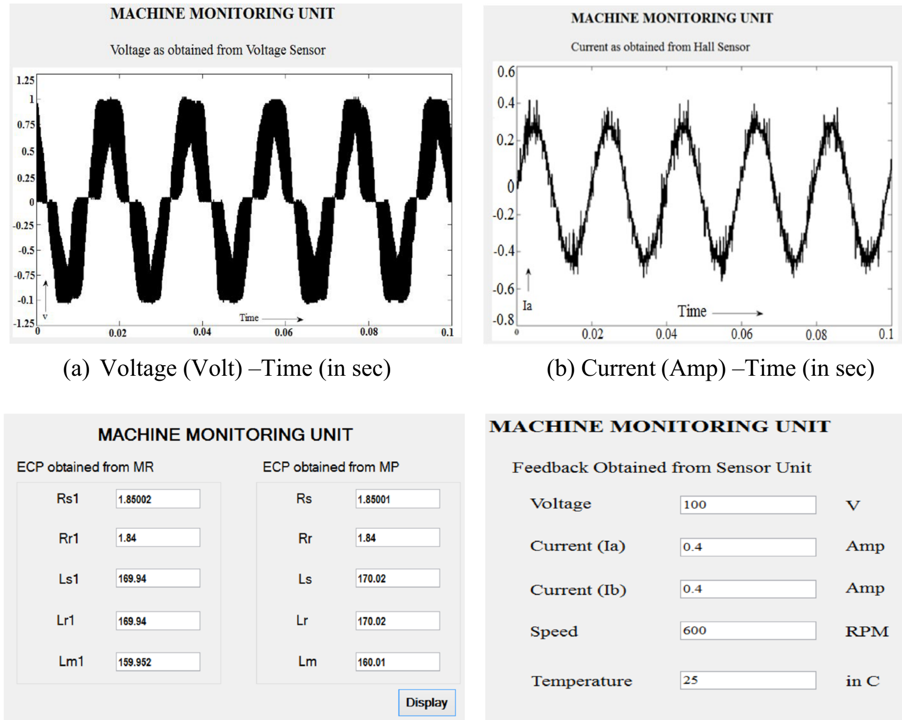

(a) Voltage (Volt) –Time (in sec) (b) Current (Amp) –Time (in sec)

(c) Evaluated ECPs (d) Evaluated values from feedback data

Fig. 19 Waveforms of sensor data for **a** voltage, **b** current, **c** evaluated ECPs and **d** evaluated values from feedback data as communicated to MMU

Table 5 ECPs obtained from the DSP-based controller

ECPs	PT test	ECPs evaluation by		ECPs evaluation by	
		simulation using ADAM optimizer	% Error	DSP Controller	% Error
R_s in Ω	1.85	1.85002	0.001	1.85002	0.001
R_r in Ω	1.84	1.84	0.00	1.8401	0.054
X_s in Ω	53.38	53.386	0.0112	53.389	0.00168
L_s in mH	170	170.02	0.0112	170.028	0.00168
L_m in mH	160	160.01	0.0062	160.0112	0.0062

close to the simulated values. The data for % error of this table justifies the avoidance of PT for the evaluation of ECPs.

Case 8: Sensorless Speed estimation

The speed of the motor is estimated without any speed sensor based on the ECPs of the motor during its running condition as well as feedback values of voltage and current following Eq. (52). The estimated speed is tabulated for a wide range of reference speeds in Table 6. The same is verified with the speed estimated using an optical sensor mounted on the rotor shaft of the motor, the waveform of which is shown in Fig. 20. The y axis of the figure here represents the amplitude of the signal obtained from the optical sensor

Table 6 Speed estimation by the proposed method

Reference speed (Nr*) in rpm	Speed estimated using proposed method (N_{r1}) in rpm	Speed evaluated by optical sensor (N_{r2}) in rpm	%Error (N_r–N_{r1})	%Error (N_r–N_{r2})
400	399.86	400	0.035	0
600	600.2	601	−0.033	0.1
800	799.71	800	0.0.3	0
1000	1000.2	1000	0.02	0
1200	1199.5	1201	0.041	0.1
1400	1400.3	1400	−0.02	0

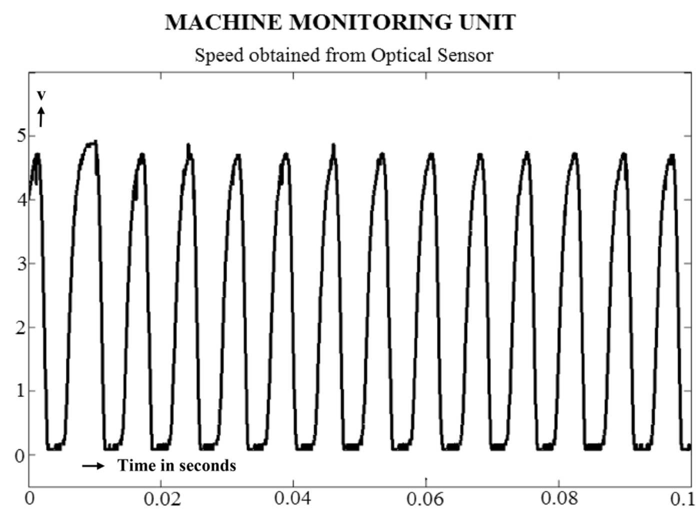

Fig. 20 MMU of VSI-IM showing speed

and the x-axis represents the time. The % error is computed for both the sensored and sensorless methods and it is observed that the sensorless method is equally applicable for speed estimation. The optical sensor has a resolution such that one complete revolution produces 60 pulses.

Conclusion

This paper elaborates on the automatic estimation of ECPs during the starting transients and running conditions of an induction motor. The result from Tables 1 and 2 reveals that the proposed scheme avoids any physical tests of the motor and applicable to all rated motors. The speed tracking errors performance shown in Figs. 8 and 9 and the convergence criteria of ECPs evaluation as shown in Figs. 10, 11, 12 and 13 prove the efficacy of the proposed H-G and Adam-based BPANN schemes. The variation in R_s and its impact on other ECPs with motor temperature is also shown in Tables 3 and 4. An intelligent SSI for R_s and sensorless speed estimation methods are adopted to incorporate the temperature and speed error correction schemes. A hardware prototype along with a PC-based GUI is developed for its standalone operation as shown in Figs. 17 and 18. The ripple in the torque or speed is reduced drastically with this BPANN controller as evident from Figs. 15 and 16. Thus the development of an intelligent controller for induction motor drive with online parameter estimation and GUI-based display facility is described.

Abbreviations

AD	Adam optimizer
AI	Artificial intelligence
ANN	Artificial neural network
ASD	Adjustable speed drive
BPANN	Backpropagation artificial neural network
CNN	Convolution neural network
DLPF	Digital low pass filter
DSP	Digital signal processing
ECP_P	Equivalent circuit parameters obtained from plant model
ECP_R	Equivalent circuit parameters obtained from the reference model
ECP_s	Equivalent circuit parameters
EKF	Extended Kalman's filter
FLC	Fuzzy logic controller
FOC	Field-oriented control
GA	Genetic algorithm
GD	Gradient descent method
GNN	Graphical neural networks
GSA	Gravitational search algorithm
GUI	Graphical user interface
IFOC	Indirect field-oriented control
IM	Induction motor
LPF	Low pass filter
LSTM	Long short term memory
MMU	Machine monitoring unit
MRAS	Model reference adaptive structure
NN	Neural network
PSD	Phase-sensitive detector
PSO	Particle swarm optimization
PT	Physical test
PWM	Pulse width modulation
RNN	Recurrent neural network
SSI	Small signal injection method
SVM	Space vector modulation
VSI	Voltage source inverter

List of symbols

B	Loss function
E	Error
f	Frequency
f_2	Lock-in signal of frequency in SSI
f_3	Refresh rate in SSI
g_n	Gradient of the error
h	Hidden layer
i_{dr}, i_{qr}	D-q axis rotor current
i_{ds}^*, i_{qs}^*	Stator reference current in the d-q axis
i_{ds}, i_{qs}	D-q axis stator current
I_{nl}	No-load current
I_r	Rotor current
I_s	Rated stator current
K	The ratio between R_s and R_r
K_1	Controller gain of the flux flow path
K_2	Controller gain of the torque flow path
K_3	Controller gain of the slip frequency
K_{pls}, K_{ils}	PI controller gain in the torque flow path
L_m	Magnetizing inductance
L_r	Rotor inductance
L_s	Stator inductance
L_{m1}	Mutual inductance of M_R
L_{r1}	Rotor inductance of M_R
L_{s1}	Stator inductance of M_R
M	Modulation index
m	Momentum term in ADAM rule
M_P	Plant model
M_R	Reference model

N_r	Rated speed
p	Number of poles
p_f	Power factor rated condition
p_{fnl}	Power factor at no load
$P_{nl}, P_{rcl}, P_{scl}, P_{out}$	No-load power, rotor copper loss, stator copper-loss, rated power
P	Active power referred to the α-β
Q	Reactive power referred to the α-β
Q_1	Reactive power in the d-q axis
R_c	Core resistance
R_r	Rotor resistance
R_{r1}	Rotor resistance of M_R
R_s	Stator resistance
R_{s1}	Stator resistance of M_R
r_n	Summation of the squared term of gradients
$r(t)$	Modulating signal of SSI
S	Activation function
s	Slip
s_m	Maximum slip
T	Temperature at start
T_e	Electromechanical torque
T_{pwm}	Time period of PWM
T_{lc}	Period of lock-in signal in SSI
t_1,t_2,t_0	Switching instances of SPWM
V_s	Rated stator voltage
V_{an}, V_{bn}, V_{cn}	Instantaneous phase voltages of VSI
v_{dc}	Dc supply voltage
v_{dr}, v_{qr}	D-q axis rotor voltage
v_{dr}, v_{qr}	D-q axis rotor voltage
v_{ds}^*, v_{qs}^*	Stator reference voltage in the d-q axis
v_r	Lock-in voltage
V_{ssi}, i_{ssi}	Voltage and current of SSI method
v_{svm}	Voltage vector of SVM
v_α, v_β	α-β Axis voltage
w_n	Current weight of nth iterations
$w_{(n+1)}$	Modified weight after nth iterations
X_m	Magnetizing reactance
x_{vbdc}, y_{vbdc}	Dc component voltage in-phase and quadrature component in SSI
Y	Output of the forward path of M_P
Y_{MP}	Output ECPs for plant model
Y_{MR}	Output ECPs for reference model
Z_{eqP}	Per phase impedance of M_P
Z_{eq}	Per phase impedance
Z_{eqR}	Per phase impedance of M_R
δ	Tolerance limit
δ_{lc}	Duty cycle in SSI
η	Learning rate
σ	Total leakage coefficient
$\psi_{ds}, \psi_{qs}, \psi_{qr}, \psi_{dr}$	D-q axis flux
ω_r	Rotor speed
ω_s	Synchronous speed
ω_{sl}	Slip Speed
τ_R	Rotor time constant

Acknowledgements
We would like to thank Mr. Rakesh Das for his generous help for development of the hardware system.

Author contributions
The theory has been developed, and also the simulation and practical verification of the work is being done by the corresponding author. Prof (Dr) J.N. Bera has supervised the entire work. Both authors read and approved the final manuscript.

Authors' information
Tista Banerjee received a B.Tech. degree in electrical engineering from Techno India in 2006, M.Tech. in electrical engineering from the University of Calcutta, in 2008. She has worked as an Assistant Professor in the College of Engineering and Management Kolaghat (2008–2009) and at B.P.Poddar Institute of Management and Technology, (2009–2017). Her research interest is on power electronics and control systems.
Jitendra Nath Bera is associated with the Department of Applied Physics of the University of Calcutta, Kolkata. He has obtained his B.Tech. and M.Tech. degrees from the University of Calcutta and Ph.D. degrees from Jadavpur University. He has more than 35 in national and international journals. His research areas include Power Electronics, Smart Grid, Electrical Machines, control system wireless communication, and Embedded Systems.

Funding
This is a self-sponsored project. There is no source of any funding for this research from any other external resources.

Availability of data and materials
The data of the motor that has been considered here are taken from the nameplate of the motor. The NEMA specifications of AC machine IEEE 112 data have also been used.

Declarations

Competing interests
The authors, Tista Banerjee and Prof. (Dr.) J.N. Bera, declare that they have no competing interests.

Received: 4 August 2021 Accepted: 25 September 2022
Published online: 17 October 2022

References

1. Bose BK (2002) Modern power electronics and AC drives. Prentice Hall, Upper Saddle River, pp 70–74
2. Odhano SA, Pescetto P, Awan HAA, Hinkkanen M, Pellegrino G, Bojoi R (2019) Parameter identification and self-commissioning in AC motor drives: a technology status review. IEEE Trans Power Electron 34(4):3603–3614
3. Tang J, Yang Y, Blaabjerg F, Chen J, Diao L, Liu Z (2018) Parameter identification of inverter-fed induction motors: a review. Energies 11(9):2194
4. Chandra BM, Prasantlr BV, Manindher KG (2018) A review on parameter estimation techniques in decoupling control of induction motor drive. In: 2018 4th international conference on electrical energy systems (ICEES), Chennai, India, 7–9 Feb. 2018. https://doi.org/10.1109/icees.2018.8443209
5. Maiti S, Chakraborty C, Hori Y, Ta MC (2008) Model reference adaptive controller-based rotor resistance and speed estimation techniques for vector controlled induction motor drive utilizing reactive power. IEEE Trans Ind Electron 55(2):594–601
6. Kan J, Zhang K, Wang Z (2015) Indirect vector control with simplified rotor resistance adaptation for induction machines. IET Power Electron 8(7):1284–1294
7. Cao P, Zhang X, Yang S (2017) A unified-model-based analysis of MRAS for online rotor time constant estimation in an induction motor drive. IEEE Trans Ind Electron 64(6):4361–4371
8. Yang S, Ding D, Li X, Xie Z, Zhang X, Chang L (2017) A novel online parameter estimation method for indirect field oriented induction motor drives. IEEE Trans Energy Convers 32(4):1562–1573
9. Zamboti Fortes M, Hugo Ferreira V, Palma Francisco Coelho A (2013) The induction motor parameter estimation using genetic algorithm. IEEE Lat Am Trans 11(5):1273–1278
10. Awadallah MA (2008) Parameter estimation of induction machines from nameplate data using particle swarm optimization and genetic algorithm techniques. Electr Power Compon Syst 36(8):801–814
11. Wu RC, Tseng YW, Chen CY (2018) Estimating parameters of the induction machine by the polynomial regression. Appl Sci 8(7):1073
12. Chaturvedi DK, Singh MP (2019) Online equivalent circuit parameter estimation of three-phase induction motor using ANN. J Inst Eng Ser B 100(4):343–347
13. Jirdehi MA, Rezaei A (2016) Parameters estimation of squirrel-cage induction motors using ANN and ANFIS. Alex Eng J 55(1):357–368. https://doi.org/10.1016/j.aej.2016.01.026
14. Wlas M, Krzeminski Z, Toliyat HA (2008) Neural-network-based parameter estimations of induction motors. IEEE Trans Ind Electron 55(4):1783–1794
15. Karanayil B, Rahman MF, Grantham C (2007) Online stator and rotor resistance estimation scheme using artificial neural networks for vector controlled speed sensorless induction motor drive. IEEE Trans Ind Electron 54(1):167–176
16. Çetin O, Dalcalı A, Temurtaş F (2020) A comparative study on parameters estimation of squirrel cage induction motors using neural networks with unmemorized training. Eng Sci Technol Int J 23(5):1126–1133
17. Dubey AK, Jain V (2019) Comparative study of convolution neural network's relu and leaky-relu activation functions. Applications of Computing, Automation and Wireless Systems in Electrical Engineering, pp 873–880
18. Kingma DP, Ba J (2014) Adam: a method for stochastic optimization. arXiv preprint arXiv:1412.6980
19. Gao Z, Habetler TG, Harley RG (2009) A complex space vector approach to rotor temperature estimation for line-connected induction machines with impaired cooling. IEEE Trans Ind Electron 56(1):239–247
20. Zhang P, Du Y, Habetler TG, Lu B (2011) Magnetic effects of DC signal injection on induction motors for thermal evaluation of stator windings. IEEE Trans Ind Electron 58(5):1479–1489
21. Ying Wu, Gao H (2006) Induction-motor stator and rotor winding temperature estimation using signal injection method. IEEE Trans Ind Appl 42(4):1038–1044
22. Sonnaillon MO, Bisheimer G, De Angelo C, García GO (2010) Online sensorless induction motor temperature monitoring. IEEE Trans Energy Convers 25(2):273–280
23. Wang H, Ge X, Yue Y, Liu Y-C (2020) Dual phase-locked loop-based speed estimation scheme for sensorless vector control of linear induction motor drives. IEEE Trans Ind Electron 67(7):5900–5912
24. Davari SA, Wang F, Kennel RM (2018) Robust deadbeat control of an induction motor by stable MRAS speed and stator estimation. IEEE Trans Ind Inf 14(1):200–209
25. Chen J, Huang J, Sun Y (2019) Resistances and speed estimation in sensorless induction motor drives using a model with known regressors. IEEE Trans Ind Electron 66(4):2659–2667
26. Zaky MS, Metwaly MK, Azazi HZ, Deraz SA (2018) A new adaptive SMO for speed estimation of sensorless induction motor drives at zero and very low frequencies. IEEE Trans Ind Electron 65(9):6901–6911

27. Benbouzid (2003) The HG diagram model for induction motors analysis: theoretical approach and applications. Electr Power Compon Syst 31(3):211–239
28. Bhowmick D, Manna M, Chowdhury SK (2018) Estimation of equivalent circuit parameters of transformer and induction motor from load data. IEEE Trans Ind Appl 54(3):2784–2791
29. Lee K, Frank S, Sen PK, Polese LG, Alahmad M, Waters C (2012) Estimation of induction motor equivalent circuit parameters from nameplate data. In: 2012 North American power symposium (NAPS), Champaign, IL, USA, 9–11 Sept. 2012. https://doi.org/10.1109/naps.2012.6336384
30. Uzair M, Jamil N (2020) Effects of hidden layers on the efficiency of neural networks. In: 2020 IEEE 23rd international multitopic conference (INMIC). IEEE. Bahawalpur, Pakistan, 5–7 Nov. 2020, pp 1–6. https://doi.org/10.1109/inmic50486.2020.9318195
31. Panchal FS, Panchal M (2014) Review on methods of selecting number of hidden nodes in artificial neural network. Int J Comput Sci Mob Comput 3(11):455–464

Publisher's Note

Springer Nature remains neutral with regard to jurisdictional claims in published maps and institutional affiliations.

Submit your manuscript to a SpringerOpen journal and benefit from:

- ► Convenient online submission
- ► Rigorous peer review
- ► Open access: articles freely available online
- ► High visibility within the field
- ► Retaining the copyright to your article

Submit your next manuscript at ► springeropen.com